

Synergistic degradation of polystyrene nanoplastics in water: Harnessing solar and water-driven energy through a Z-scheme SnO₂/g-C₃N₄/PVDF-HFP piezo-photocatalytic system

Arezou Fazli ^{a,*}, Simone Lauciello ^b, Rosaria Brescia ^b, Ricardo Carzino ^c, Athanassia Athanassiou ^a, Despina Fragouli ^{a,*}

^a Smart Materials, Istituto Italiano di Tecnologia, via Morego 30, Genova 16163, Italy

^b Electron Microscopy Facility, Istituto Italiano di Tecnologia, via Morego 30, Genova 16163, Italy

^c Materials Characterization Facility, Istituto Italiano di Tecnologia, via Morego 30, Genova 16163, Italy



ARTICLE INFO

Keywords:

Water treatment
Z-scheme photocatalysts
Renewable energy sources
Solar light
Plastic

ABSTRACT

The rise of nanoplastics (NPs) as a water pollutant poses threats to aquatic ecosystems and human health. This study presents an approach that combines solar and water-driven energy sources with advanced materials to degrade NPs. For this purpose, a SnO₂/g-C₃N₄/PVDF-HFP piezo-photocatalyst has been developed. The SnO₂/g-C₃N₄ photocatalyst with Z-Scheme charge transfer demonstrates high activity under simulated solar light. Simultaneously, ultrasound waves, employed to mimic water motion, serve to activate the piezoelectric properties of g-C₃N₄, thereby enhancing charge separation. Moreover, the immobilization of SnO₂/g-C₃N₄ onto piezoelectric poly (vinylidene fluoride-co-hexafluoropropylene) (PVDF-HFP) nanofiber mats augments its piezocatalytic efficiency and prevents dispersion in the reaction media. During the piezo-photocatalytic process, generated reactive species attack polystyrene (PS) NPs and introduce oxygen-based functional groups. This leads to surface corrosion, fragmentation, and 46 % mineralization in just 15 h under mild conditions, outperforming existing literature. Overall, this research emphasizes the importance of harnessing renewable energy sources for NP remediation.

1. Introduction

Inadequate waste management results in the accumulation of substantial amounts of plastic in natural ecosystems [1]. Presently, around 13 million tons of plastic are being discharged into aquatic environments annually, with projections indicating that by 2025 nearly 250 million tons will be present in aquatic systems, raising significant concerns about water pollution [2]. Larger plastic objects entering water bodies degrade into smaller particles in the micrometric and nanometric size range (microplastics, MPs, and nanoplastics, NPs) due to weathering, bio-, photo-, and thermal degradation processes [3]. MPs and NPs can also originate from primary sources coming from industries processing plastic or from their release from cosmetic, textiles and personal care products, to name some [3,4].

Despite limited information on environmentally relevant concentrations, sizes, and compositions of NPs, estimations suggest their presence in natural water bodies at concentrations ranging from 0.0003

to 8.6 mg L⁻¹ [5–9]. This raises significant ecological concerns for aquatic organisms, soil biota, and human health even at such very low, environmentally relevant concentrations [10]. NPs, due to their small size, can easily enter the food chain, posing adverse effects on living systems by permeating cell membranes and accumulating in various organs [11–13]. Furthermore, NPs can sorb hazardous organic and inorganic compounds [10], like persistent organic pollutants and heavy metals, thanks to their surface chemistry and high surface-to-volume ratio [3]. These substances can be then unwittingly transferred and released to the various accumulation sites in the biological systems, as recent studies on *in vitro* and *in vivo* models have proved [14,15].

Various advancements have been made to combat environmental contamination caused by NPs and MPs. In addition to up-to-date regulations that prohibit single-use plastics, encourage the adoption of biodegradable alternatives, and restrict the utilization of primary MPs in diverse products to address the root causes [16], there are also strategies that focus on mitigating the presence of the existing MPs and NPs within

* Corresponding authors.

E-mail addresses: Arezou.Fazli@iit.it (A. Fazli), Despina.Fragouli@iit.it (D. Fragouli).

the environment [17]. These methods include microbial degradation [18], adsorption [19], electro-sorption [20], and coagulation [21]. However, each approach has its limitations, such as difficulty in large-scale implementation or only partial transformation of nanoparticles rather than complete elimination. Therefore, alternative methods need to be explored to effectively mitigate NPs pollution in aqueous environments.

Advanced oxidation processes (AOPs) offer a promising solution for NPs removal. AOPs utilize oxidative reactions to generate highly reactive oxygen species (ROS), such as hydroxyl radicals ($\cdot\text{OH}$), which attack and break down NPs. In particular, heterogeneous photocatalysis in water is emerging as a particularly effective technique within AOPs for degrading and mineralizing NPs. Paul Henri Allé et al. [22] investigated the degradation of polymethylmethacrylate nanobeads with particle size of 105 nm using TiO_2 -P25/ β -SiC foams and UV-A radiation. The carbon content in the nanobeads decreased by approximately 50% within 7 hours of treatment. In another study, an immobilized $\text{Cu}_2\text{O}/\text{CuO}$ semiconductor degraded PS NPs (size of 350 nm), under visible light irradiation, resulting in a 23 % reduction in the concentration (% w/v) of PS NPs and 15 % mineralization after 50 hours of treatment [23]. Furthermore, TiO_2 photocatalyst structures were explored for photo-degradation of 315 nm PS NPs achieving a degradation efficiency of 23.5 % after 50 hours of UV irradiation [1]. However, a critical examination of these studies reveals certain limitations. These include a predominant reliance on UV light, extended reaction times, exceeding 40 hours, and the requirement for low pH values, below 5. Furthermore, the investigations have utilized photocatalysts in powder form, posing challenges in tracking the degraded NPs and necessitating additional post-processing steps for catalyst recovery. These factors emphasize the need for extensive research efforts for a more realistic, highly efficient and rapid NPs degradation process, especially utilizing renewable and readily available energy sources, such as sunlight and water waves.

A promising component for such type of application is graphitic carbon nitride ($\text{g-C}_3\text{N}_4$). $\text{g-C}_3\text{N}_4$ is a metal-free semiconductor, which possesses a moderate bandgap suitable for absorbing visible light. In its undoped, original, form it exhibits a high recombination rate of the photogenerated charges [24]. Nonetheless, it has been proved that the heterojunction formed between $\text{g-C}_3\text{N}_4$ and an n-type semiconductor, such as SnO_2 , effectively mitigates charge recombination, thereby augmenting its photocatalytic activity [25]. Furthermore, recent research has revealed that $\text{g-C}_3\text{N}_4$ possesses a non-centrosymmetric hole in its tri-s-triazine layer structures, which gives rise to in-plane piezoelectricity [24]. The piezoelectric property enables $\text{g-C}_3\text{N}_4$ to convert mechanical energy into a piezoelectric field [26,27]. This built-in piezoelectric field imparts a compelling force to circumvent the recombination of photo-induced electron-hole pairs of $\text{g-C}_3\text{N}_4$, thereby increasing their lifespan and the overall photocatalytic performance [28]. Although the synergistic combination of all these factors holds significant potential for enhancing the photocatalytic efficiency of $\text{g-C}_3\text{N}_4$, the so-far utilized components primarily exist in powdered form posing several challenges.

With the present research, we aim to address all these issues, through the development of a highly efficient Z-scheme piezo-photocatalyst for the degradation of PS NPs using renewable energy resources, with virtues of good solar light absorption ability, attractive piezoelectricity, and easy recovery. In this regard, a Z-scheme $\text{SnO}_2/\text{g-C}_3\text{N}_4$ heterostructure with improved solar light absorption and reduced electron-hole recombination was synthesized and characterized. To facilitate the recoverability of the photocatalyst and enhance the catalytic performance, we immobilized the $\text{SnO}_2/\text{g-C}_3\text{N}_4$ heterostructure onto a flexible and piezoelectric PVDF-HFP nanofibrous substrate. In contrast to other nonfunctional substrates, PVDF-HFP has evolved into a valuable substrate that not only effectively supports photocatalysts but also, thanks to its flexibility, converts water flow fluctuations into a piezoelectric field [29]. Consequently, this transformation positively influences the separation of photo-induced charges within the

photocatalysts, thereby enhancing the overall photocatalytic performance [29]. We prove that both simulated solar light and water flow oscillations, generated by ultrasound waves, activate the piezoelectric and photocatalytic properties of the $\text{SnO}_2/\text{g-C}_3\text{N}_4$ heterostructure. The presence of the PVDF-HFP nanofiber mat enhances the piezocatalytic performance by creating a piezoelectric field that facilitates charge separation within the $\text{SnO}_2/\text{g-C}_3\text{N}_4$ heterostructure and enhances the degradation of PS NPs. Additionally, it effectively immobilizes the $\text{SnO}_2/\text{g-C}_3\text{N}_4$ nanopowder and prevents its dispersion in the reaction media. To the best of our knowledge, this study represents the first report exploring the utilization of piezo-photocatalytic processes for NPs degradation, paving, thus, the way for mitigating NPs pollution in aqueous environments through the utilization of renewable energy sources.

2. Experimental section

2.1. Chemicals

Tin(II) chloride dihydrate ($\text{SnCl}_2 \cdot 2 \text{H}_2\text{O}$, CAS number: 10025–69–1, purity 98 %); ammonium hydroxide solution (NH_4OH , CAS number: 1336–21–6); melamine ($\text{C}_3\text{H}_6\text{N}_4$, CAS number: 108–78–1, purity 99 %); ammonium chloride (NH_4Cl , CAS number: 12125–02–9); poly(vinylidene fluoride-co-hexafluoropropylene) (PVDF-HFP, CAS number: 9011–11–0); N, N-dimethylformamide (DMF, CAS number: 68–12–2, purity 99.80 %); 1,4-benzoquinone ($\text{C}_6\text{H}_4\text{O}_2$, 99%), iso-butanol ($\text{C}_4\text{H}_{10}\text{O}$, 99.5 %), formic acid (CH_2O_2 , >95 %, CAS number: 64–18–6); silver nitride (AgNO_3 , >99.99 %, CAS number: 7761–88–8); terephthalic acid ($\text{C}_6\text{H}_4(\text{COOH})_2$, 98 %, CAS number: 100–21–0, and acetone (CAS number: 67–64–1, purity 99.5 %) were purchased from Sigma Aldrich and used as received, without further purification. Colloidal PS NPs with a diameter of 100 nm and a concentration of 10 mg mL⁻¹ were acquired from Alpha Nanotech.

2.2. Preparation of the piezo-photocatalyst

SnO_2 nanoparticles were synthesized using a simple co-precipitation method [30]. Initially, a solution of $\text{SnCl}_2 \cdot 2 \text{H}_2\text{O}$ (3 g) in 100 mL of double-distilled water was stirred for one hour at room temperature (RT) until a clear solution was formed. Subsequently, 8 M aqueous ammonia was gradually added to adjust the pH to 9. The resulting solution was stirred for one hour at RT, leading to the formation of a white precipitate. The precipitate was allowed to undergo undisturbed nucleation for 24 hours. Afterward, the suspension underwent centrifugation at a relative centrifugal force (RCF) of 21460 xg, utilizing distilled water to remove impurities. The obtained precipitate was dried at 80 °C for 4 hours and subsequently calcined at 500 °C for 4 hours. The resulting off-white color powder was collected for further characterization.

The synthesis of 2D $\text{g-C}_3\text{N}_4$ was carried out using the following approach described by Lei et al. [31]. Accordingly, melamine powder (4.0 g) and NH_4Cl (16 g) were thoroughly mixed and ground. The mixture was then heated in a crucible covered with aluminum foil at 550 °C for 4 hours with a heating rate of 6 °C/min. After cooling to RT, the resulting yellow solid was collected and stored for subsequent use.

To prepare the $\text{SnO}_2/\text{g-C}_3\text{N}_4$ composite with a theoretical $\text{SnO}_2:\text{g-C}_3\text{N}_4$ weight ratio of 1:1, the as-prepared $\text{g-C}_3\text{N}_4$ was dispersed in milliQ water and subjected to one hour of sonication to obtain a homogeneous suspension. The synthesis method used for SnO_2 , as described above, was then applied to the $\text{g-C}_3\text{N}_4$ suspension. To promote the SnO_2 growth, the resulting composite was calcined at 400 °C.

PVDF-HFP nanofibers were prepared by dissolving 2.162 g of PVDF-HFP pellets in a mixture of DMF and acetone (6:4 vol ratio, 10 mL). The solution was stirred for 3 hours at 70 °C until complete dissolution. Subsequently, it was magnetically stirred overnight to ensure homogeneity. The resulting solution was then loaded into a Becton Dickinson

syringe (5 mL) with an 18 GA blunt tip needle and placed to a syringe pump (NE-1000, New Era Pump Systems, Inc., NY, USA). A vertical electrospinning was used to electrospun the fibers on the aluminum collector placed at a distance of 25 cm, while a voltage of 27 kV was applied (EH40R2.5, Glassman High Voltage, Inc., US-NJ, USA). The optimal electrospinning parameters included a flow rate of 500 $\mu\text{L h}^{-1}$, a temperature range of 21–23°C, and a relative humidity of 46–56 %. The as-prepared nanofiber mat was used as the substrate for spraying the previously prepared $\text{SnO}_2/\text{g-C}_3\text{N}_4$ heterostructure powder. For doing this, 0.031 g of the $\text{SnO}_2/\text{g-C}_3\text{N}_4$ powder was dispersed in 10 mL of ethanol and sonicated for one hour to achieve a homogeneous dispersion. The resulting suspension was sprayed onto the prepared PVDF-HFP mat (0.051 g) using a spray gun (Paasche Airbrush, U.S.A) at a distance of 10 cm and a pressure of 2.0 bar. The $3 \times 3 \text{ cm}^2$ surface of the PVDF-HFP nanofibers was sprayed for five consecutive times, and a hot air gun at a temperature of 50 °C was used after each spraying cycle to facilitate drying. After five cycles of spraying, the samples were left to dry overnight at ambient conditions and the weight of the final material was measured. The deposition of the $\text{SnO}_2/\text{g-C}_3\text{N}_4$ heterostructure onto the PVDF-HFP resulted in a 0.031 g of weight gain of the mat. This additional weight corresponds to the $\text{SnO}_2/\text{g-C}_3\text{N}_4$ particles attached to the PVDF-HFP (60.78 %wt with respect to the total weight of the PVDF-HFP mat). Finally, the obtained composite system was washed with milliQ water five consecutive times, and then immersed in milliQ water and subjected to sonication to remove any non-attached particles from the fibrous mats surface. The residual water, in which the mat underwent such treatment, was subjected to a comprehensive analysis. This assessment aimed to detect any possible detachment of the heterostructure from the PVDF-HFP mat. The analysis was performed using a UV-VIS-NIR spectrophotometer (Varian Cary 5000), and dynamic light scattering (DLS, Zetasizer Nano S, Malvern Instruments). We observed through the absorption and DLS spectra, that following a two-hour sonication period, no detachment of $\text{SnO}_2/\text{g-C}_3\text{N}_4$ occurred from the composite mats.

2.3. Piezo-photocatalytic experiments

The piezo-photocatalytic activity of the synthesized samples was evaluated for the degradation of PS NPs under RT and ambient pressure conditions. A solar simulator was used to provide high-intensity and uniform illumination on a target spot area of 14.14 cm^2 . The solar flux of 1 Sun, equivalent to the standard AM 1.5 G (AM: air mass) conditions defined by ASTM E927–05 standards, corresponding to 100 mW cm^{-2} was used for the irradiation in air, at ambient conditions. To introduce vibration energy and promote the movement of the PS NPs in the suspension, an ultrasonic bath operating at 59 kHz and 100 W was employed. The water temperature of the bath was consistently monitored using a thermometer, and any potential rise was mitigated by adding ice to the water.

The piezo-photocatalytic experiments were conducted in a 250 mL beaker. Initially, 100 mL of PS NPs dispersion with a concentration of 100 ppm was added to the beaker. The $\text{SnO}_2/\text{g-C}_3\text{N}_4/\text{PVDF-HFP}$ mat was positioned within a square holder, submerging it at the center of the solution to enhance its interaction with the PS NPs. Nevertheless, it was loosely fixed, allowing the PVDF-HFP nanofibers to deform and stimulate their piezoelectric behavior. Afterwards, the piezo-photocatalytic degradation process was initiated in the presence of ultrasound waves and simulated solar light irradiation. It is important to highlight that, for comparison reasons, both the photocatalytic and piezocatalytic processes were also carried out separately, following the same procedure. In particular, in the case of the photocatalytic process, no ultrasound was present, while in the piezocatalytic process, the simulated solar light irradiation was not taking place. At different time intervals up to 15 h, 250 μL of the treated samples were collected from the reactor for further analysis. In order to separate the aqueous medium from the suspended PS NPs, the collected samples were subjected to centrifugation

(Centrisart® G-16 C, RCF of 21460 xg). The solid portion was separated from the liquid and both components were used for further characterizations.

2.4. Characterization methods

X-ray diffraction (XRD) measurements were performed using a Malvern PANalytical Empyrean instrument. The XRD setup included a 1.8 kW Cu K α ceramic X-ray tube and a PIXcel3D 2 × 2 area detector, operating at 45 kV and 40 mA. The samples were placed on a zero-diffraction silicon wafer for the measurements. The comparison of the XRD patterns with the reference PDF files is depicted in Figs. S1 (a) and (b). XRD patterns were also utilized to estimate the interplanar spacing and crystallite size of the samples through the Bragg's law and Scherrer equation, respectively [32].

In order to examine the chemical groups of the samples, we utilized an attenuated total reflection (ATR) accessory (MIRacle ATR, PIKE Technologies) coupled with an FTIR spectrometer (Vertex 70 v FTIR, Bruker). By averaging 64 repetitive scans, we acquired ATR-FTIR spectra within the range of $4000\text{--}500 \text{ cm}^{-1}$. These spectra were recorded with a resolution of 4 cm^{-1} and all spectra were normalized. In case of the PS NPs, the oxidation degree before and after the degradation process was assessed through the carbonyl index (CI) calculation. In particular, the CI was calculated by considering the unchanged out-of-plane =C-H bending at 696 cm^{-1} as the reference peak, and the peak referred to the -C=O bond at 1734 cm^{-1} . The CI index was determined using the formula: $\text{CI} = I_{\text{C=O}} / I_{\text{C-H}}$, where I represents the intensity of the corresponding peaks.

The absorbance spectra for the PS NPs suspension were obtained using a Varian Cary 5000 UV-visible-NIR spectrophotometer. The same instrument, equipped with the corresponding solid sample holder, was employed to measure the absorbance of the as-synthesized catalysts. The results were subsequently employed to estimate the optical band gap of SnO_2 , $\text{g-C}_3\text{N}_4$, and $\text{SnO}_2/\text{g-C}_3\text{N}_4$, utilizing the Tauc equation as previously outlined [33,34]. Ultraviolet photoelectron spectroscopy (UPS) analysis was employed to determine the work function (Φ) of the catalysts. Accordingly, a Kratos Axis UltraDLD spectrometer with a He I (21.22 eV) discharge lamp was used. The measurements were performed on a $55 \mu\text{m}$ diameter area with a pass energy of 10 eV and a dwell time of 100 ms. To precisely determine the low kinetic energy cut-off, a bias of -9.0 V was applied to the sample. The Φ of the samples were calculated using the formula $\Phi = h\nu - (E_{\text{Fermi}} + E_{\text{cutoff}})$, with the He I energy ($h\nu$) set at 21.22 eV [35]. The valence band (VB) positions of SnO_2 and $\text{g-C}_3\text{N}_4$ were determined through X-ray photoelectron spectroscopy (XPS) analysis. For the as-prepared materials, a Kratos Axis UltraDLD spectrometer (Kratos Analytical Ltd., UK) equipped with a monochromatic Al K α source ($h\nu = 1486.6 \text{ eV}$) was operated at 20 mA and 15 kV. The analysis covered an area of $300 \times 700 \mu\text{m}^2$. High-resolution spectra were obtained with a pass-energy of 10 eV and an energy step of 0.1 eV. The conduction band (CB) positions of the samples were calculated using the following formula $E_{\text{CB}} = E_{\text{VB}} - E_g$, where E_{CB} , E_{VB} , and E_g denote the energy level of the CB, VB, and band gap energy, respectively [36].

On the other hand, for the PS NPs, XPS analysis was conducted using an electron spectrometer (Lab2, Specs, Berlin, Germany) equipped with a monochromatic X-ray source set at 1486 eV. The analysis utilized a hemispherical energy analyzer (Phoibos, HSA3500, also from Specs), and the Al K α X-ray source operated at an applied voltage of 13 kV and an applied current of 8 mA. The analysis chamber maintained a pressure of approximately $1 \times 10^{-9} \text{ mbar}$. Wide and narrow scans were performed in the large-area lens mode. The wide scan employed energy pass and step settings of 90 eV and 1 eV, respectively. For the narrow high-resolution scan, energy pass and step settings were adjusted to 30 eV and 0.1 eV, respectively. A flood gun was used to neutralize the surface charge, with an energy of 7 eV and a filament current of 2.2 A. Data analysis was carried out using CasaXPS software (Casa Software, Ltd., version 2.3.22). It is worth noting that samples preparation was

conducted under the same conditions, while XPS analysis was performed on all samples at the same day to ensure consistency and comparability. For the analysis of the elemental contributions, the O amount attributed to the indium oxide substrate was excluded from the analysis as described in the [supporting information](#) section S1.

Scanning electron microscope (SEM) analysis was conducted using a Zeiss GeminSEM 560 (Zeiss, Oberkochen, Germany), equipped with a field-emission gun, at acceleration voltages ranging from 1.5 to 5.0 kV. The microscope is equipped with an Oxford XMax-80 SDD detector for EDS analyses. The high-resolution sputter coater, Cressington 208HR, manufactured by Cressington Scientific Instrument Ltd., UK, was employed for the coating processes. A 10 nm thick layer of gold (Au) was applied to the SnO₂, g-C₃N₄, SnO₂/g-C₃N₄, and SnO₂/g-C₃N₄/PVDF-HFP samples prior to analysis. In the case of PS NPs, a 10 nm thick layer of carbon coating was applied using the same equipment.

Transmission electron microscopy (TEM) analysis was performed by drop-casting dispersions of the powder samples onto a holey carbon-coated Cu grid. Overview bright-field TEM (BF-TEM) imaging was carried out on a JEOL JEM-1400Plus instrument, operated at 120 kV. High-resolution TEM (HR-TEM) imaging was conducted using an image-Cs-corrected JEOL JEM-2200FS TEM operated at 200 kV, equipped with a direct electron detection (DED) camera (Gatan K2 Summit). In order to minimize carbon contamination and beam damage, HRTEM images were acquired in low-dose-rate conditions. The HRTEM images reported here are extracted from (260 nm)² images obtained from the sum of 40 cross-correlated frames, each of them exposed for 0.3 s at a dose rate of 30 e⁻/Å²/s. Elemental analyses of the samples were carried out using the same microscope in STEM-EDS mode, employing a Bruker X-Flash 5060 SDD detection system. For more information please refer to the [supporting information](#) section S2. STEM-EDS maps were obtained by integrating the K α peak for C, N, and O, and the L α peak for Sn. The Image J software was used to facilitate the computation of the mean particle size and standard deviation.

Nanoparticle tracking analysis (NTA) was performed on a Nano-tracker Nanosight NS300 (Malvern Panalytical). To achieve this, the collected samples were diluted by a factor of 100 in ultrapure water, subjecting them to 3 minutes of vortexing before injecting them into the instrument at a consistent flow rate. Additionally, the surface charge of the samples was measured through zeta potential analysis using a Zetasizer Nano S (Malvern Instruments) spectrometer.

To follow the fate of PS NPs after the piezo-photocatalytic process, total organic carbon (TOC) was measured using a membraPure uniTOC lab analyzer. As a control experiment, we repeated the same process in the absence of the PS NPs to monitor the potential release of organic compounds from our catalysts. The collected samples were injected to the instrument without prior centrifugation. The TOC present in the solution was oxidized using a UV/persulfate procedure, resulting in the transformation of TOC into CO₂, which was subsequently quantified by non-dispersive infrared spectroscopy. The percentage of mineralization resulting from the degradation processes was calculated using equation ([Eq. 1](#)). Three measurements were conducted and for each case the mean value was presented.

$$\text{Mineralization}(\%) = \frac{(\text{TOC}_{\text{initial}} - \text{TOC}_{\text{final}})}{\text{TOC}_{\text{initial}}} \times 100 \quad (1)$$

We used an AFM (Asylum Research MFP3D) for the piezoelectric response force microscopy (PFM) measurements, set in single frequency mode. A NSC36/Cr-Au tip with an estimated spring constant of $k \approx 0.6 \text{ N m}^{-1}$ was used. AC modulation voltage (V_{ac}) of 3 V was applied to the AFM tip during scan in contact to obtain PFM images of a single PVDF nanofiber fixed on top of a SiC substrate. In addition, the piezoelectric properties of the materials were qualitatively assessed on an Instron 3365 dynamometer, equipped with compression anvils and a 2 KN load cell. Samples were sandwiched between tin foil/copper tape electrodes, which were connected to a Keithley 2612B Sourcemeter to measure the current generated upon mechanical cues. Quick compress-

release cycles were applied to the samples in displacement control with the rate of 1 mm min⁻¹, until reaching the imposed maximum pressure of 0.7 MPa, before releasing the force down to 1/10 of the maximum value. The time needed for each cycle was between 3 and 5 seconds, depending on the specific thickness and stiffness of each sample. For each test were performed 50 cycles. Current was measured throughout the tests with a frequency of approximately 10 Hz. Supplementary tests were carried out on paper as a negative control sample to ensure the accuracy of the current measurements and to rule out any potential artifacts. The photoluminescence (PL) spectra of the solid samples were collected using a Fluoromax®-4 Spectrofluorimeter. To perform the transient photocurrent response and electrochemical impedance spectroscopy (EIS) tests, we employed an individual-channel potentiostat MultiPalmSens with software MultiTrace. Pt wire served as the counter electrode, while an Ag/AgCl electrode functioned as the reference electrode. The electrolyte solution utilized in these experiments consisted of 0.5 mol L⁻¹ Na₂SO₄. We used ITO glass substrates for the working electrodes. First, the ITO surfaces were cleaned with acetone, water, and ethanol, followed by a 2 min plasma treatment to ensure surface activation. Then, we dispersed materials in ethanol and sprayed them onto the ITO. For the composite with PVDF, we electrospun a thin layer of PVDF-HFP solution onto the ITO before spraying SnO₂/g-C₃N₄ suspension. All samples were placed in an oven to evaporate residual solvents and firmly attach the material onto the ITO substrate. The prepared working electrodes were then utilized for the subsequent analyses.

The formation of •OH during different degradation processes was studied by the acquired PL spectra. For this purpose, terephthalic acid (TA) was used as the probe molecule. TA exhibits no inherent fluorescence; however, its interaction with the generated •OH during the degradation processes results in the production of fluorescent 2-hydroxyterephthalic (TAOH), with excitation at 315 nm. To initiate the experiment, a 5×10^{-4} mol L⁻¹ aqueous solution of TA was prepared in a basic solution containing 2×10^{-3} mol L⁻¹ of NaOH. The catalyst was added to 100 mL of the prepared TA solution and underwent irradiation with ultrasound or the simulated solar light, depending on the specific degradation process under investigation. It is important to highlight that, for all experiments conducted an equivalent photocatalyst quantity (0.031 g) was employed both in powdered form and loaded onto the PVDF-HFP mat. Subsequently, the PL spectra were recorded using a Fluoromax®-4 Spectrofluorimeter. To investigate the role of photo-generated electron-hole pairs in the production of •OH in the SnO₂/g-C₃N₄ heterostructure, AgNO₃ and formic acid were added to the solutions as the electron and hole scavengers, respectively.

Furthermore, the generation of various reactive species such as •OH, superoxide (•O₂) radicals, electron, and hole during the piezo-photocatalytic process was investigated by introducing different scavengers [[37,38](#)]. For this purpose, iso-butanol (IBA), 1,4-benzoquinone, (BQ), AgNO₃, and formic acid were used as the appropriate •OH, •O₂, electron, and hole scavengers, respectively. To achieve this, the degradation of caffeine, as a readily traceable water pollutant, in the presence of scavengers and under the same conditions employed for the degradation of PS NPs was monitored. The efficiency of caffeine degradation (DE %) was calculated using the equation $\frac{C_0 - C_t}{C_0} \times 100$, where C₀ and C_t represent the initial and residual concentration of caffeine at time 't', respectively. It is essential to note that the scavenger to caffeine concentration ratio was maintained at 10:1 in the reactions.

3. Results and discussion

3.1. Physicochemical characterization of the developed materials

XRD patterns of the as-synthesized SnO₂, g-C₃N₄, and their heterostructure were acquired to investigate their crystal structures and potential interfacial interactions. Given [Fig. 1](#) and [Fig. S1](#), the XRD patterns

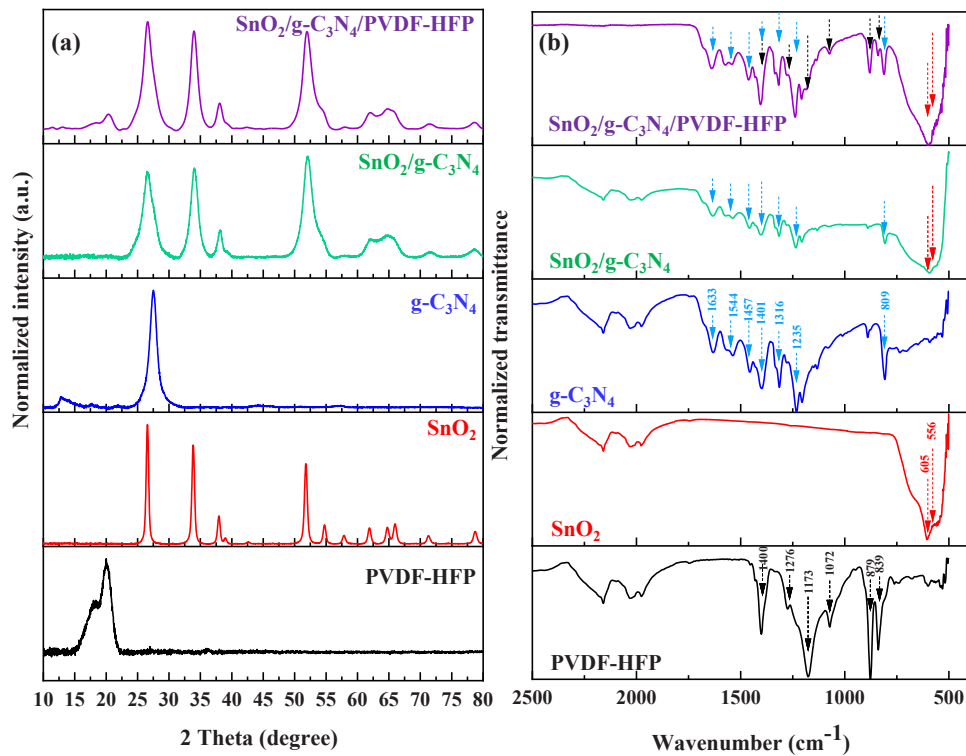


Fig. 1. (a) XRD patterns and (b) FTIR spectra of the prepared materials. The XRD patterns closely align with the reference ICSD card numbers: #84576 for SnO₂ and #194747 for g-C₃N₄.

for all samples exhibit well-defined peaks, indicating the presence of crystalline phases. The SnO₂ pattern shows characteristic peaks, which correspond to the SnO₂ tetragonal phase (PDF 98–008–4576) for the particles, with a crystallite size of 16.5 ± 0.9 nm as depicted by the Scherrer equation (Table S2). No additional peaks are observed, indicating their high phase purity. The XRD analysis of g-C₃N₄ reveals two prominent peaks in the obtained pattern, which resembles the orthorhombic structure for a slightly hydrogenated phase (C₂₄N₃₀(NH₂)₆) reported by Fina et al. [39] (PDF 01–083–7340). The highest intensity peak is observed at $2\theta = 27.65^\circ$, attributed to the (002) planes, corresponding to the interplanar stacking of the conjugated aromaticity within the g-C₃N₄ structure [24]. The peak at 12.78° (210), corresponding to (210) planes, represents the tri-s-triazine unit in g-C₃N₄. These distinct peaks provide evidence of the crystalline nature of the as-synthesized g-C₃N₄, with a crystallite size of 4 ± 1 nm (Table S2).

Upon forming the SnO₂/g-C₃N₄ heterostructure, the XRD pattern exhibits the characteristic peaks of both SnO₂ and g-C₃N₄, signifying the preservation of their individual crystalline structures. Notably, no additional peaks are observed, confirming the absence of impurities or secondary phases. Additionally, the diffraction peaks that correspond to the SnO₂, grown on the pre-existing g-C₃N₄ flakes, are broader compared to the peaks of the individual SnO₂ particles. Correspondingly, the average crystallite size was reduced to 6 ± 2 nm. The crystallite size reduction for SnO₂ nanoparticles within the SnO₂/g-C₃N₄ composite can be attributed to the utilization of a lower calcination temperature for the formation of the heterostructure [40].

Once the SnO₂/g-C₃N₄ heterostructure was fixed on the PVDF-HFP mats, no alterations on the characteristic peaks corresponding to SnO₂ and g-C₃N₄ were observed. This is also the case for the PVDF-HFP diffraction pattern, which shows two partially superimposing peaks, one at 18.1° that corresponds to the α phase, and the other at 20.1° attributed to the β phase of the polymer, which plays a crucial role in its piezoelectric behavior [41]. The conservation of the peaks' position in the composite material confirms that the inclusion process of the SnO₂/g-C₃N₄ heterostructure to the PVDF-HFP mat does not affect the

crystalline phase of the polymer, thereby preserving the β phase and its inherent piezoelectric behavior.

The FTIR spectra of the developed materials are presented in Fig. 1(b) and Fig. S2 (a). In reference to the FTIR spectrum of SnO₂, the presence of a broad peak at approximately 607 cm^{-1} indicates the formation of an oxide-bridge functional group (Sn-O-Sn) [42]. Furthermore, the successful oxidation of Sn and dehydration of SnO₂ subsequent to calcination at 600°C is supported by the absence of peaks within the ranges of $3394 - 3409\text{ cm}^{-1}$ (corresponding to the O-H bond) and $1620 - 1630\text{ cm}^{-1}$ (associated with water) [42,43]. This indicates that the calcination process effectively removed the hydroxyl groups and water molecules from the particles. In the case of the g-C₃N₄, the discernible peak at 809 cm^{-1} indicates the presence of triazine units. Moreover, the characteristic peaks at 1235 , 1316 , 1401 , 1457 , and 1544 cm^{-1} correspond to the C-N heterocyclics, while the C=N stretching mode was evidenced by the peak at 1633 cm^{-1} [44]. The FTIR spectrum of the SnO₂/g-C₃N₄ heterostructure reveals distinctive peaks associated with both SnO₂ and g-C₃N₄. Notably, the peaks corresponding to Sn-O-Sn bonds exhibit a blue shift, shifting to higher wavenumbers by approximately 12 cm^{-1} . This change indicates the interaction between the components during the SnO₂ growth on g-C₃N₄. Similar shifts in FTIR spectra have been observed in previous studies as well [45].

Concurrently, the crystalline phases of the prepared PVDF-HFP nanofibers were further scrutinized through FTIR spectroscopy. Distinctive peaks were discerned at wavenumbers 879 , 1072 , 1173 , 1276 , and 1400 cm^{-1} , which correspond to C-C, C-F, and C-F₃ vibrations within PVDF [46]. The presence of the α -phase was ascertained by the peak at 1400 cm^{-1} , while the β -phase crystals in PVDF were indicated by the peaks at 1277 cm^{-1} and 839 cm^{-1} [46]. Significantly, as evident from Fig. 1(b) and Fig. S2 (b), the composite mat of SnO₂/g-C₃N₄/PVDF-HFP successfully encapsulates all distinctive peaks associated with SnO₂/g-C₃N₄ and PVDF-HFP. It is worth noting that the peaks corresponding to the C-N heterocyclics of g-C₃N₄ and α -phase of PVDF overlap in the SnO₂/g-C₃N₄/PVDF-HFP sample. Nonetheless,

considering also the XRD analysis of Fig. 1(a), we can safely conclude that the composite mat maintains the integrity of both the α -phase and β -phase of the PVDF nanofibers.

The morphology of the developed components were analyzed by electron microscopy as presented in Fig. S3. In accordance with previous studies, following similar fabrication methods as the ones presented herein [25], the synthesized SnO_2 nanoparticles exhibit a spherical morphology with a mean particle size of 50 ± 10 nm (Figs. S3 (a-c) and Fig. S4). On the other hand, the $\text{g-C}_3\text{N}_4$ exhibits a distinctive two-dimensional flake-like structure characterized by layers (Figs. S3 (e-g)). The $\text{SnO}_2/\text{g-C}_3\text{N}_4$ reveals the SnO_2 nanoparticles grown on the surface of the $\text{g-C}_3\text{N}_4$ flakes, suggesting the successful formation of the heterostructure (Fig. 2(a) and Figs. S3 (i-k)). The STEM-EDS mapping confirms that SnO_2 nanoparticles are dispersed over the $\text{g-C}_3\text{N}_4$ fragments within the $\text{SnO}_2/\text{g-C}_3\text{N}_4$ heterostructure sample (Fig. S5). The HRTEM analysis of the $\text{SnO}_2/\text{g-C}_3\text{N}_4$ heterostructure (Fig. 2(a), Fig. 2 (b-e), and section S2), reveals the presence of porous flake-like features in the sample. Moreover, SnO_2 is observed within these flake-like features, indicating direct contact between SnO_2 and $\text{g-C}_3\text{N}_4$ structures. Both SnO_2 and $\text{g-C}_3\text{N}_4$ exhibit crystalline features characterized by nanometer-sized domains; however, no well-defined relationship was observed between the respective orientations of SnO_2 and $\text{g-C}_3\text{N}_4$. These findings suggest the presence of a complex interface between the two components within the heterostructure.

Fig. 2(f) and (g) show the SEM images of the pure PVDF-HFP fibers revealing their consistently smooth surface. Given Fig. S4, the majority

of fibers exhibit an average diameter of 377.0 ± 6.5 nm. Electrospraying the $\text{SnO}_2/\text{g-C}_3\text{N}_4$ particles on the PVDF-HFP mats results in their homogeneous distribution on the fibers as depicted with the elemental mapping images in Fig. S6 and Figs. 2(i) and (j). Fig. S7 presents additional cross-section SEM images of the final composite mats that provide further evidence of the penetration of the $\text{SnO}_2/\text{g-C}_3\text{N}_4$ heterostructure into the mats, with a higher concentration on the upper surface and a lower concentration on the bottom surface. It is important to highlight that, as indicated in the inset of Fig. 2(k), the composite fibrous mat is still flexible allowing its deformation, which is favorable for piezophotocatalytic reactions.

Analyzing the UV-vis absorption data presented in Fig. S8 (a), the distinct contributions of SnO_2 and $\text{g-C}_3\text{N}_4$ can be observed in the $\text{SnO}_2/\text{g-C}_3\text{N}_4$ system. Specifically, in the heterostructure's spectrum can be observed two absorption peaks attributed to the (i) SnO_2 , in the ultraviolet (UV) region of the spectrum, and (ii) $\text{g-C}_3\text{N}_4$ to the visible light region up to 500 nm. The determination of the average band gap was performed using the Tauc plot (Figs. S8 (b) to (d)) and the Kubelka-Munk formula [33,34]. The obtained E_g values for SnO_2 , $\text{g-C}_3\text{N}_4$, and $\text{SnO}_2/\text{g-C}_3\text{N}_4$ were 3.78, 2.87, and 2.92 eV, respectively. These results, in accordance with previous studies, [47] provide compelling evidence that the $\text{SnO}_2/\text{g-C}_3\text{N}_4$ heterostructure demonstrates enhanced light capture capabilities at longer wavelengths, addressing the limited absorption range of pure SnO_2 . Moreover, as previously reported, [47] the incorporation of SnO_2 in the heterostructure is expected to significantly improve photo-induced charge separation, thereby overcoming the poor

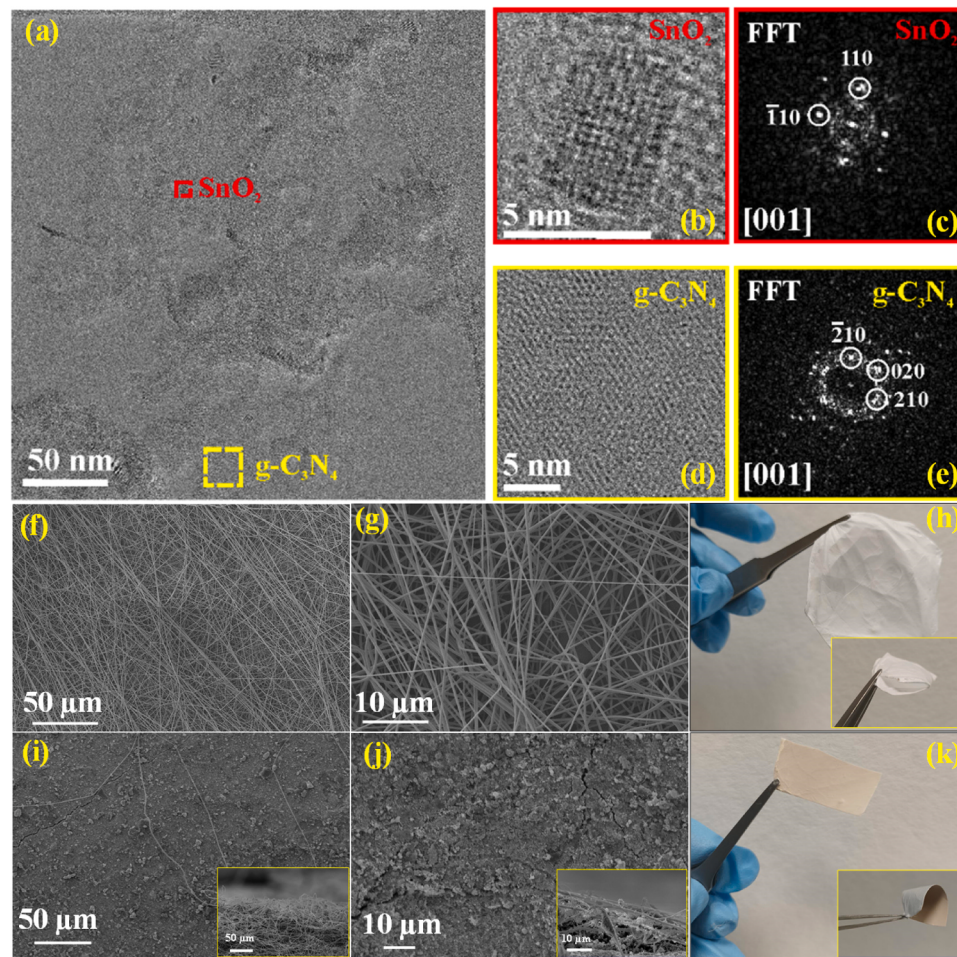


Fig. 2. (a) Overview TEM image of a fragment in the $\text{SnO}_2/\text{g-C}_3\text{N}_4$ material and (b-e) corresponding HRTEM and FFT patterns for a SnO_2 particle (indexed according to ICSD 84576 structure) and a region within $\text{g-C}_3\text{N}_4$ (indexed based on ICSD 194747 structure). Additionally, SEM images and photos of (f-h) pure PVDF-HFP and (i-k) $\text{SnO}_2/\text{g-C}_3\text{N}_4/\text{PVDF-HFP}$ are included. Insets of i and j: the cross-section images of the mats. Insets of h and k indicate the flexibility of the mats.

photocatalytic activity of g-C₃N₄. It should be noted the SnO₂/g-C₃N₄ heterostructure fixed on the PVDF-HFP mat retained the same absorbance properties as its powdered form.

To gain insight into the charge separation mechanism within the SnO₂/g-C₃N₄ heterostructure, the energy levels of both components were investigated. The VB positions of SnO₂ and g-C₃N₄ were determined through XPS valence spectra, as shown in Fig. S9 (a-b) respectively. Based on the analysis, the VB positions were found to be 3.64 and 0.61 eV for SnO₂ and g-C₃N₄, respectively. Given the obtained VB and E_g, the CB was calculated to be -0.14 and -2.26 eV for SnO₂ and g-C₃N₄, respectively. The band edge positions of SnO₂ and g-C₃N₄, along with further analysis (presented in detail at the [supporting information](#) Section S3), confirmed that their surface contact induce an internal electric field, facilitating Z-scheme charge separation upon irradiation. Therefore, the highly potential electrons in the CB of g-C₃N₄ and the holes in the VB of SnO₂ are spatially separated, leading to intense redox reactions. Wang et al. [48], and He et al. [25] have also proposed the Z-scheme charge separation mechanism for the B-doped g-C₃N₄/SnS₂ and SnO_{2-x}/g-C₃N₄, respectively.

3.2. Piezo-photocatalytic degradation of PS NPs

Fig. 3 illustrates the SEM images of the NPs both before and after a 15 h of photocatalytic, piezocatalytic, and piezo-photocatalytic degradation processes. As shown, in comparison to the sole photocatalytic and piezoelectric processes, the piezo-photocatalytic process exhibits a higher destructive impact on PS NPs. In particular, contrary to the relatively smooth surface of the NPs observed after the separate photocatalytic and piezocatalytic processes, in the combined piezo-photocatalytic process it is evident their surface erosion and their fragmentation in smaller particles in the range of few nanometers (see also [supporting information](#) Fig. S11). Such nanofragments were observed as isolated particles, but also in the form of aggregates. To ascertain that the fragments observed were not derived from the g-C₃N₄/SnO₂ heterostructure that possibly could detach from the PVDF-HFP nanofibers during the reaction, the EDS and elemental dot mapping of the PS NPs collected after 15 hours of the piezo-photocatalytic process have been conducted (**Fig. S12**), revealing no indication of the presence of the

photocatalyst. Furthermore, UV-vis spectra of the PS NPs dispersions before and after the piezo-photocatalytic process (**Fig. S13**) indicate only the presence of the polymer with a characteristic peak within the range of 200–290 nm, attributed to the presence of benzene rings or ethylbenzene [49]. Therefore, our findings provide confirmation of the presence of PS NPs both before and after the degradation process, while simultaneously verify the absence of any released photocatalyst in the reaction media. Consequently, we may conclude that the observed minute particles originate from the degradation of PS NPs. Jiang et al. [50] reported similar findings, which confirmed the presence of cracks and voids on PS MPs following the photocatalytic degradation process in the presence of CuMgAlTi-LDH photocatalyst.

NTA analysis, provides further evidences on the particles modification after the adopted degradation processes (**Fig. S14**). The concentration/size distribution profiles displayed in the figures reveal distinct characteristics. In the case of pristine PS NPs, two peaks are evident: one corresponding to particles with a size of 103 nm (representing the individual particles) and a smaller peak at 234 nm, likely indicating PS NPs aggregates. After the various degradation processes, new peaks emerge, with a greater number observed in the context of the piezo-photocatalytic process. Upon normalizing the acquired concentration (number of particles mL⁻¹), we calculated the percentage ratio of the newly formed particles to the remaining pristine PS NPs, and these results are reported in **Fig. S15**. Notably, after 15 h of piezo-photocatalytic process, PS NPs undergo further erosion, leading to the formation of smaller particles in the range of 40 nm, 51 nm, or even smaller, as well as aggregation events resulting in larger particles with sizes of 183 nm, 217 nm, and 345 nm. The existence of these new peaks can be attributed to the generation of nanofragments through surface erosion of the NPs during the degradation process and to their potential aggregation either with each other or with the larger remaining NPs.

The decrease in the repulsion forces among the dispersed NPs can contribute to their propensity for aggregation [51]. To comprehend the alterations in the NPs interactions caused by piezo-photocatalytic degradation, the surface charge of the differently processed NPs was studied through zeta potential analysis (**Fig. S16**). As observed, the piezo-photocatalytic degradation process induced a shift in the zeta potential towards less negative values, a phenomenon possibly

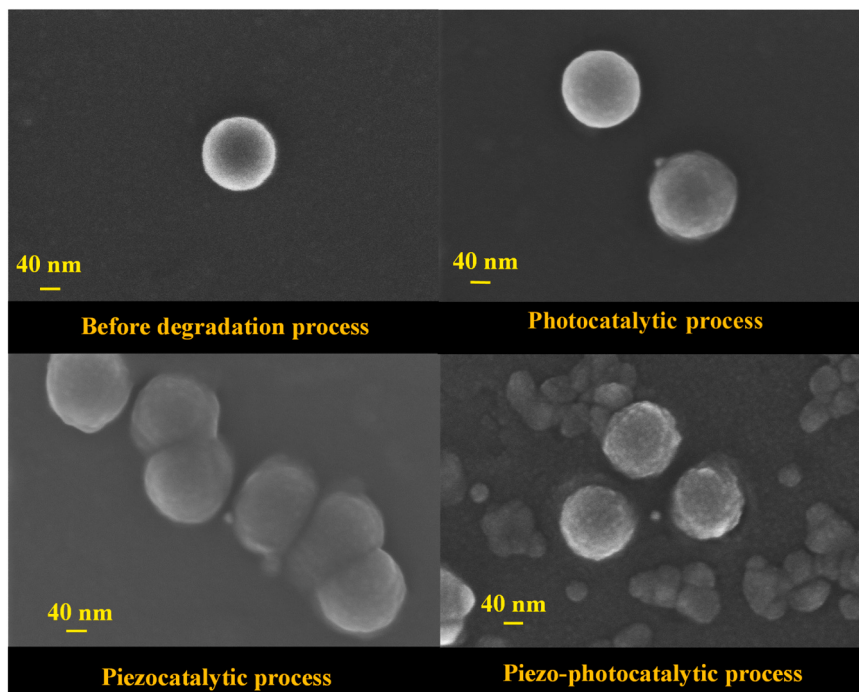


Fig. 3. SEM images of PS NPs before and after 15 h of the photocatalytic, piezocatalytic, and piezo-photocatalytic degradation processes.

attributed to the appearance of oxygen functional groups on the surface of the particles, specifically hydroxyl, ether, and carbonyl groups. These functional groups undergo protonation and remain uncharged at neutral pH, leading to a less negative charge on the surface of the NPs. This is also confirmed by Bhagat et al. [51] who reported the significance of surface modifications and the subsequent alterations in surface charge properties during the aging process of PS NPs. They observed a shift towards less negative zeta potential values in response to the production of oxygen functional groups during the aging process.

To investigate the chemical composition variation of the PS NPs caused by a 15-hour piezo-photocatalytic process, FTIR analysis was employed (Fig. S17). As shown the pristine PS NPs exhibit distinct bands corresponding to the aromatic C–H (at 3025, 3060, and 3081 cm⁻¹), aliphatic C–H (at 2921 and 2851 cm⁻¹), aromatic C=C stretching vibrations (at 1601, 1491, and 1449 cm⁻¹), and C–H bending vibrations of the aromatic rings (at 905, 752, and 696 cm⁻¹) [52]. These characteristic peaks were also observed in the FTIR spectrum of the PS NPs after 15 hours of piezo-photocatalytic degradation, indicating the preservation of the polymer's basic chemical structure during the process.

A closer look to the signals in the 1400–1900 cm⁻¹ region, Fig. 4(a), illustrates the presence of C=O bonds with the emerging peak at 1746 cm⁻¹ in the pristine PS NPs. This can be attributed to the oxidation of PS NPs during their preparation and storage procedure. However, interestingly, these impurities could play a role as initiators for the subsequent polymer chain oxidation [53]. The observed peak remained consistently stable, with the CI remaining almost negligible (close to 0) throughout both the photocatalytic and piezocatalytic processes. However, after 15 h of the piezo-photocatalytic process, an increase in C=O stretching vibrations is observed, inducing a CI change from 0.019 to 0.036, indicating a 1.9-fold increase. At the same time, the C=O peak exhibited both broadening and a shift from 1746 cm⁻¹ to 1736 cm⁻¹. These findings suggest the efficient introduction of oxygen-based components to the PS NPs, and especially of various C=O-containing functional groups, including ketones, ethers, esters, and aldehydes. However, the absence of peaks related to the O–H stretching vibrations (3600–3200 cm⁻¹) suggests that these carbonyl groups cannot be attributed to the presence of carboxylic acids. Furthermore, based on Fig. S17(b), the absence of a main characteristic peak at the range of 2700–2800 cm⁻¹, the range of C–H bonds in aldehydes, in the spectrum of the treated PS NPs indicates that the peak at 1734 cm⁻¹ cannot be attributed to the presence of aldehydes. Therefore, the potential oxidation products may include ketones, ethers, and esters [53]. Moreover, the presence of ketones signifies that a breakage has occurred in the original polymer chain.

A study by Domínguez-Jaimes et al. [1] investigated the degradation of PS NPs using anodized TiO₂, a commonly used photocatalyst for water contaminants. Their study revealed that an exposure to UV light of a photocatalyst area of 1 cm² in the presence of PS NPs (concentration of 0.9 % w/v) and a reaction time of 50 hours, induced a 3.1-fold CI increase, from 0.088 to 0.275. Even if the CI increase is higher compared to the one of the present study, it should be stressed that our research is based on solar and water-driven energy harnessing to degrade PS NPs, rather than the UV used in the reported study [1] while the degradation process is conducted in a shorter timeframe (15 hours instead of 50 hours [1]). Furthermore, the concentration of PS NPs in our process was approximately 11 times higher, while the exposed photocatalyst area 9 times larger than that of the referenced study. As a result, our findings strongly support the potential of the piezo-photocatalytic process as a promising method for degrading nanoparticles.

In Fig. S18, wide-scan XPS spectra of PS NPs both before and after undergoing the different degradation processes are presented. These results reveal an initial O/C peak area ratio of 0.005 for untreated PS NPs. However, this ratio significantly increases after the photocatalytic, piezocatalytic, and the piezo-photocatalytic treatment reaching 0.070, 0.160, and 0.160 respectively, suggesting that all three oxidation processes induce the presence of oxygen containing groups on the surface of

PS NPs. Interestingly, these results diverge from the CI analysis previously performed, which indicates better activity for the piezo-photocatalytic process and nearly no activity in the production of oxygen-based functional groups on PS NPs under the other catalytic processes. Considering that XPS investigates the chemical composition of only a few nanometers of thickness, we can conclude that all three processes initiate oxidation reactions from the surface [53]. However, as successfully revealed by the FTIR analysis, when compared to the other processes the piezo-photocatalytic process appears to be capable of oxidizing even deeper layers. This can be attributed to the enhanced efficiency of the prepared piezo-photocatalyst in generating free radical species, which are available for driving oxidation reactions.

Additionally, Fig. 4(b-e) display the corresponding high-resolution C1s spectra of the samples. The deconvolution of C 1 s for the pure PS NPs, demonstrates the presence of peaks at 284.80, 285.24, 286.84, and between 290.00 and 292.00 eV corresponding to aromatic and aliphatic carbon, to C–O, and to π → π* shake-up, respectively [54]. The same peaks were observed for the PS NPs after 15 hours of the photocatalytic, piezocatalytic, and piezo-photocatalytic processes. Further investigation was conducted by evaluating the π → π* shake-up which is the characteristic of aromatic rings in PS NPs. The deconvolution of the π → π* shake-up signal observed in the pure PS NPs revealed the presence of three distinct sub-peaks. These sub-peaks correspond to various electron transition modes within the aromatic ring system [54,55]. However, after the oxidation processes two sub-peaks with shifted peak positions appear for the π → π* shake-up satellite. These changes could be attributed to several factors, including changes in the chemical composition of PS NPs and subsequently to the electronic structure of the sample. Since the sub-peak located at 291.60 eV appears both in the pristine PS NPs and at the samples collected after different degradation processes, we use this peak as the reference peak to evaluate the ratio of C_{aliphatic}/π → π*. From the analysis presented in the insets of Fig. 4, it is evident the reduction in atomicity of PS NPs and the more efficient introduction of oxygen-based functional groups in the presence of the piezo-photocatalytic process. These findings are consistent with a previous study by Li et al. [56], where it was reported that following the ozonation of PS NPs, the peak at 291.0 eV disappears and distinctive characteristic peaks attributed to oxygen species emerge.

Furthermore, as previously detailed, PS NPs underwent oxidation, leading to erosion. Therefore, this process may give rise to diverse by-products that could be released into the reaction medium. While our forthcoming work aims for a comprehensive investigation of the produced intermediates and by-products, we conducted TOC analysis to thoroughly evaluate the efficacy of the degradation process. TOC analysis provides a foundational understanding of how reactive species contribute to breaking down both PS particles and any associated organic by-products. To achieve this, we collected samples before and after each process, which ran for 15 hours, and analyzed them directly, without performing any separation process. This direct analysis allowed us to establish a clear correlation between the measured TOC values and the concentration of organic carbon originating from both the PS NPs, and the by-products resulting from their degradation. Fig. S19 illustrates the mineralization efficiency following 15 h of various degradation processes. As shown, for photocatalytic and piezocatalytic processes the efficiency is almost the same (10.1 % and 11.5 %, respectively). The mineralization efficiency in the combined piezo-photocatalytic process increased to 46.6 %, marking a 2.1-fold improvement over the sum of the results obtained from the individual processes. Therefore, our findings demonstrate the synergistic effect of the piezo-photocatalytic process in achieving efficient mineralization by exploiting the simulated green energy sources, while aligning with the promising outcomes reported by other researchers. Table S3 details the experimental conditions and findings of research studies closely aligned with our own. Accordingly, García-Muñoz et al. [52] reported the highest mineralization (80 %) of PS NPs (140 nm) employing immobilized photocatalysts. However, this rate of mineralization is achieved under 96 hours of UVA

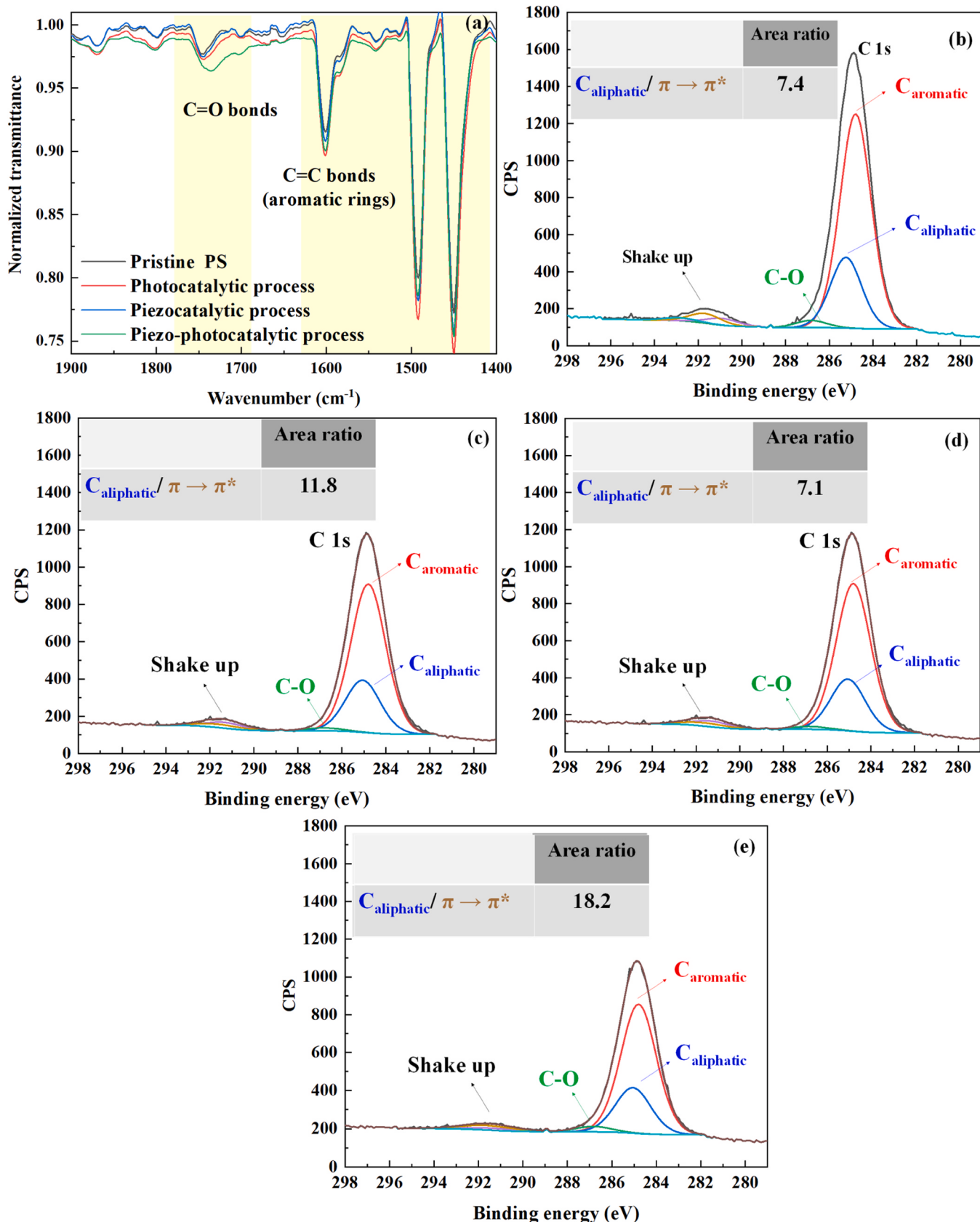


Fig. 4. FTIR spectra of PS NPs: (a) enlarged region between 1400–1900 cm^{-1} . High-resolution XPS spectra of C1s of (b) pristine, and treated PS NPs after 15 h of (c) photocatalytic, (d) piezocatalytic, and (e) piezo-photocatalytic processes.

irradiation. Nonetheless, in our study achieved 46.6 % mineralization in a much shorter timeframe of just 15 hours using simulated solar and water-driven energy sources. It is worth noting that a control experiment was conducted to analyze the TOC of the samples in the absence of PS NPs during the piezo-photocatalytic process. However, the TOC was found to be similar to that of the milli-Q water used, confirming the absence of any potential release of organic compounds from our piezo-photocatalyst.

Hence, our results demonstrate that the piezo-photocatalytic process exhibits higher activity in the degradation and mineralization of PS NPs compared to processes involving individual piezocatalytic and photocatalytic components. It is worth noting that the degradation process, for the specific time duration, did not induce any significant changes at the crystallographic and chemical properties of the material, as illustrated in **Figs. S20 (a-b)** of the [supporting information](#). The observed enhanced performance can be attributed to the induced piezoelectric field attributed to the PVDF-HFP nanofibrous substrate, which plays a crucial role in promoting the efficient separation of photo-induced electron-hole pairs, consequently elevating the overall photocatalytic effectiveness [38,57]. In fact, it is widely established that the manipulation of PVDF-HFP nanofibers through ultrasonic vibration or other mechanical energy sources induces deformation and spontaneous polarization [58]. This is also proved by specific tests on the herein fabricated PVDF-HFP fibrous mats. Specifically, as shown in **Fig. S21**, in the PFM single-frequency scan conducted by applying AC voltage through the conductive AFM cantilever tip to a single PVDF-HFP nanofiber, a 260 pm amplitude shift was observed on top of the fiber. Though the equation $A=d_{33}V_{ac}Q$, where A is the piezoelectric amplitude, Q denotes the quality factor, and d_{33} the piezoelectric coefficient, d_{33} was determined to be 8.6 pm/V, aligning closely with values reported in prior studies for the PVDF-HFP nanofibers [59,60]. In addition, **Fig. S22**, depicts the piezoelectric output signals of the PVDF-HFP nanofibrous mats. During the rapid compress-release cycles, the mat exhibits current signals that peaked at approximately 13 nA. To ensure the reliability of the current measurements, additional tests were conducted on paper, serving as a negative control sample and helping to rule out any potential artifacts in the measurements. The results presented in **Fig. S22** indicate an absence of current in the case of the paper, further supporting the validity of the observed signals in the PVDF-HFP nanofiber experiments.

It is widely known that the built-in piezoelectric field of PVDF-HFP nanofibers can induce the migration of positive and negative charges toward opposing surfaces. When this piezoelectric field is synergistically combined with the photocatalytic system, it facilitates the mobility of photo-induced charge carriers and decrease the recombination of electron-hole pairs [28]. This prolonged lifespan of the charge carriers allows for the heightened utilization of photo-generated electrons and holes in the degradation process of PS NPs. Nonetheless, although the PVDF-HFP piezoelectric efficiency was successfully evaluated through the above-mentioned measurements, our setup was unsuitable for assessing the charge dynamics under the light irradiation.

To assess the efficiency of piezoelectric field in transfer and separation of photogenerated charges, we conducted tests involving transient photocurrent response, electrochemical impedance spectroscopy (EIS), and PL spectra analysis on the samples. **Fig. 5(a-b)** shows that upon simulated solar light irradiation, a negligible photocurrent generation in pure SnO_2 , moderate photocurrent in $\text{g-C}_3\text{N}_4$, and enhanced photocurrent in the $\text{SnO}_2/\text{g-C}_3\text{N}_4$ composite component was observed. As expected, when examining the response of $\text{SnO}_2/\text{g-C}_3\text{N}_4/\text{PVDF-HFP}$ substrate, the photocurrent is comparable to the composite structure alone. Interestingly, as depicted in **Fig. 5(b)**, upon subjecting these two systems to simultaneous light irradiation and ultrasound, a significant enhancement in photocurrent is observed for the $\text{SnO}_2/\text{g-C}_3\text{N}_4/\text{PVDF-HFP}$ sample. In both cases the photocurrent increase was accompanied by noticeable noise, likely stemming from the slight detachment of the catalyst from the working electrode during the ultrasonic treatment, as

also noted in previous studies [61,62]. Nonetheless, this amplification in current for the $\text{SnO}_2/\text{g-C}_3\text{N}_4/\text{PVDF-HFP}$ sample is attributed to the impact of the piezoelectric field generated in PVDF-HFP by ultrasonic vibrations, potentially intensifying the separation of photoinduced charges in $\text{SnO}_2/\text{g-C}_3\text{N}_4$.

As shown in **Fig. 5(c)**, the EIS Nyquist diagrams of the samples under different processes were analyzed to evaluate the charge transfer resistance at the semiconductor-electrolyte interface. The obtained equivalent circuit model (inserted in **Fig. 5(c)**) consists of electrolyte resistance (R_s), charge transfer resistance at the electrolyte-electrode interface (R_{ct}), and constant phase element (CPE). According to the results presented in **Table S4**, a significant decrease was observed in the presence of $\text{SnO}_2/\text{g-C}_3\text{N}_4/\text{PVDF-HFP}$ and light, and this reduction is even more under combined light and ultrasound irradiation. Therefore, in the presence of piezo-photocatalytic process there is higher interfacial carrier transfer ability, aligning well with the transient photocurrent response.

Moreover, the photoluminescence measurements of both pure PVDF-HFP and $\text{SnO}_2/\text{g-C}_3\text{N}_4/\text{PVDF-HFP}$ were conducted (**Fig. S23**). The results show a higher PL intensity for pure PVDF-HFP compared to $\text{SnO}_2/\text{g-C}_3\text{N}_4/\text{PVDF-HFP}$, indicative of a pronounced occurrence of charge carrier recombination. The reduced PL intensity in the case of $\text{SnO}_2/\text{g-C}_3\text{N}_4/\text{PVDF-HFP}$ suggests a more efficient charge movement and effective separation of charges within the composite system. Consistent findings have been documented by Liao et al. [63], demonstrating that the incorporation of $\text{Cu}_3\text{B}_2\text{O}_6$ in PVDF-HFP led to suppressed recombination of electron-hole pairs and, consequently, to a reduced PL intensity.

Additional research was undertaken to elucidate the photocatalytic activity of SnO_2 , $\text{g-C}_3\text{N}_4$, $\text{SnO}_2/\text{g-C}_3\text{N}_4$, and $\text{SnO}_2/\text{g-C}_3\text{N}_4/\text{PVDF-HFP}$ and the positive impact of the induced piezoelectric field in enhancing charge carrier separation and their contribution in generating reactive radical species. To achieve this goal, in all cases the generation of $\cdot\text{OH}$ was monitored by analyzing the PL spectra of $\text{TA}\cdot\text{OH}$, a fluorescent compound formed through the interaction of TA with the produced $\cdot\text{OH}$. In **Fig. 5(d)** and **Fig. S24**, the changes in PL signals of aqueous solutions of TA upon the various degradation processes and the different as-prepared materials are illustrated. **Fig. S24** demonstrates that the photocatalytic process in the presence of SnO_2 exhibits minimal production of hydroxyl radicals, while $\text{g-C}_3\text{N}_4$ significantly increases the PL signal. This enhancement is attributed to the $\text{g-C}_3\text{N}_4$ appropriate light absorption capability of the simulated solar light compared to SnO_2 . Combining with the ultrasound irradiation results in a slight increase of the photocatalytic activity of the $\text{g-C}_3\text{N}_4$, while under sole piezocatalytic conditions no significant $\cdot\text{OH}$ production was observed. This improvement in the combined light and ultrasound irradiation is attributed to the generation of a piezoelectric field in $\text{g-C}_3\text{N}_4$ when exposed to external mechanical forces, enhancing charge separation and reducing recombination rates, ultimately leading to more effective $\cdot\text{OH}$ radical production, in accordance with previous studies [31]. Concerning the $\text{SnO}_2/\text{g-C}_3\text{N}_4$ heterostructure, under the piezo-photocatalytic condition, the PL intensity further increased due to the effective combination of SnO_2 and $\text{g-C}_3\text{N}_4$, allowing the heterostructure to efficiently utilize a broader range of wavelengths while reducing the recombination rate of photo-generated electrons and holes. As a result, a higher number of electrons and holes actively participate in the redox reactions, leading to the elevated $\cdot\text{OH}$ radical production (**Fig. S24**).

Moreover, as shown in **Fig. 5(d)**, under piezo-photocatalytic process, the PL intensity of $\text{TA}\cdot\text{OH}$ produced by the $\text{SnO}_2/\text{g-C}_3\text{N}_4/\text{PVDF-HFP}$ heterostructure surpassed those observed in individual photocatalytic and piezocatalytic processes. The higher $\cdot\text{OH}$ production can be attributed to the effective combination of SnO_2 and $\text{g-C}_3\text{N}_4$, allowing the heterostructure to reduce the recombination rate of photo-generated electrons and holes. In addition, as illustrated in the schematic figure (**Fig. 5(e)**), the spontaneous polarization resulting from the deformation of PVDF-HFP and $\text{g-C}_3\text{N}_4$ in the presence of ultrasound waves is another

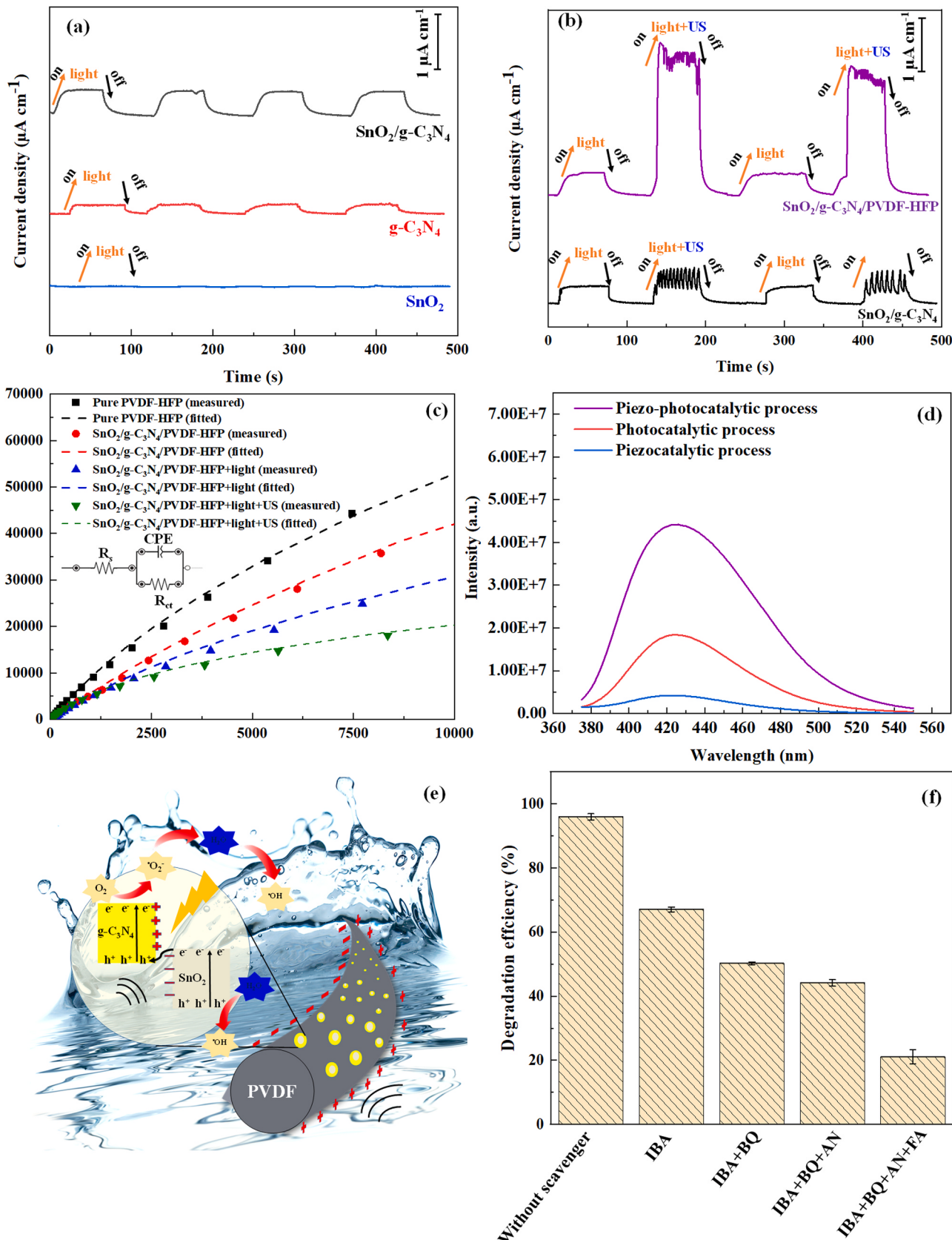


Fig. 5. (a-b) The current signal curves and (c) the EIS Nyquist plots of the sample under light and ultrasound (US) irradiation. (d) Fluorescence spectra of the generated $\text{TA}^{\bullet}\text{OH}$ during different degradation processes, (e) schematic figure of the piezo-photocatalytic process, and (f) investigation of the impact of various radical scavengers, including iso-butanol (IBA), benzoquinone (BQ), AgNO_3 (AN), and formic acid (FA), on the degradation efficiency of caffeine after 2 h of piezo-photocatalytic process.

advantage for promoting enhanced charge mobility and preventing their recombination. Therefore, the polarized electric field can be appropriately linked with the built-in electric field of $\text{SnO}_2/\text{g-C}_3\text{N}_4$ heterostructure. This synergy between the two electric fields facilitates efficient charge carrier separation, thereby enhancing the generation of reactive radical species [64].

The contribution of different reactive species, including $\cdot\text{O}_2$, $\cdot\text{OH}$, h^+ , and e^- , in the piezo-photocatalytic degradation reactions was also explored [38]. It is widely proved that the small size and high surface area of NPs enable them to adsorb various organic compounds. The adsorption of compounds such as scavengers can pose a challenge in accurately monitoring alterations in NP behavior resulting from interactions with reactive oxygen species. Consequently, to avoid any confusion, caffeine was used as a soluble pollutant to serve as a simpler model pollutant for more straightforward experiments. For this purpose different radical scavengers were utilized to monitor the degradation performance under the piezo-photocatalytic process. As illustrated in the Fig. 5(f), the degradation of caffeine reached 95% in the absence of any scavenger. However, when IBA was introduced, serving as an $\cdot\text{OH}$ scavenger, the efficiency of caffeine degradation dropped to approximately 67%, evidencing the contribution of $\cdot\text{OH}$ in the proposed piezo-photocatalytic system. To identify the role of superoxide radicals ($\cdot\text{O}_2$) in the degradation process, BQ was employed as an appropriate scavenger. With reported rate constants of 1.2×10^9 and $9 \times 108 \text{ M}^{-1} \text{ S}^{-1}$ for the reactions of BQ with $\cdot\text{OH}$ and $\cdot\text{O}_2$, respectively, BQ demonstrated its capability to scavenge both radicals [38,65]. Consequently, the addition of IBA led to quench $\cdot\text{OH}$, leaving BQ to react with $\cdot\text{O}_2$. Based on these results we may conclude that $\cdot\text{O}_2$ was generated during the piezo-photocatalytic process and took role in pollutant degradation. Furthermore, the decrease in caffeine degradation efficiency was observed in the presence of AgNO_3 and formic acid, serving as an electron and hole scavenger respectively, indicating the participation also of these reactive species in the degradation reactions. Therefore, based on the obtained results, $\cdot\text{OH}$, $\cdot\text{O}_2$, h^+ , and e^- could play the important role in the piezo-photocatalytic degradation of the polymer chains of PS NPs [66].

4. Conclusion

In summary, in a world grappling with the rising menace of NPs as a significant water pollutant, this study is believed to bring insight in the innovative approach to combat this global issue. In this regard, the herein presented Z-scheme $\text{SnO}_2/\text{g-C}_3\text{N}_4/\text{PVDF-HFP}$ piezo-photocatalyst represents a step towards sustainable NPs remediation. By incorporating ultrasound waves to simulate natural water motion, we effectively activate the piezoelectric properties of the composite, leading to improved photo-induced charge separation. In addition, the immobilization of this heterostructure onto flexible and piezoelectric PVDF-HFP nanofibers further boosts photocatalysis efficiency while ensuring the stability of the photocatalyst within the reaction medium. Notably, the morphological and size distribution analysis unveil the surface erosion and fragmentation of PS NPs into smaller particles, and elucidate their interactions. Chemical studies underscore the successful introduction of oxygen-based functional groups onto the surface of PS NPs, reaffirming the efficiency of the degradation process. The proposed process results in a mineralization efficiency of 46.6 % after 15 hours of interaction, which is 2.1-fold more than the sum of results from the individual processes.

Furthermore, unlike other papers published on the photocatalytic degradation of NPs, our research employs diverse characterization methods, such as XPS and NTA, to trace the oxidation and fragmentation of NPs, offering promising avenues for future research in this field. In conclusion, the proposed piezo-photocatalytic system offers a promising sustainable approach to mitigate the environmental impact of PS NPs, using the power of renewable energy sources. Future work will improve this proof-of-concept system by evaluating the produced by-products

and its performance in degrading various types of environmental relevant NPs within complex environmental conditions.

CRediT authorship contribution statement

Rosaria Brescia: Writing – review & editing, Methodology, Visualization, Formal analysis, Data curation. **Ricardo Carzino:** Methodology. **Simone Lauciello:** Methodology. **Athanassia Athanassiou:** Writing – review & editing, Funding acquisition. **Despina Fragouli:** Writing – review & editing, Validation, Supervision, Project administration, Conceptualization, Methodology. **Arezou Fazli:** Writing – original draft, Visualization, Methodology, Investigation, Formal analysis, Data curation, Conceptualization.

Declaration of Competing Interest

The authors declare that they have no known competing financial interests or personal relationships that could have appeared to influence the work reported in this paper.

Data Availability

No data was used for the research described in the article.

Acknowledgements

The authors extend their gratitude to Mirko Prato for conducting the UPS analysis, Luca Ceseracciu for his valuable contribution in the piezoelectric tests, Matteo Lorenzoni for his expertise in performing the PFM analysis, and Michele Ferri and Sanjana Auditto for assisting in the electrochemical tests. In addition, we thank Dr. Barbara Mazzolai for providing the required solar simulator for our experiments.

Appendix A. Supporting information

Supplementary data associated with this article can be found in the online version at doi:10.1016/j.apcatb.2024.124056.

References

- [1] L.P. Domínguez-Jaimes, E.I. Cedillo-González, E. Luévano-Hipólito, J.D. Acuña-Bedoya, J.M. Hernández-López, Degradation of primary nanoplastics by photocatalysis using different anodized TiO_2 structures, *J. Hazard. Mater.* 413 (2021) 125452, <https://doi.org/10.1016/j.jhazmat.2021.125452>.
- [2] A.A. Mohana, S.M. Farhad, N. Haque, B.K. Pramanik, Understanding the fate of nano-plastics in wastewater treatment plants and their removal using membrane processes, *Chemosphere* 284 (2021) 131430, <https://doi.org/10.1016/j.chemosphere.2021.131430>.
- [3] Y. Gong, Y. Bai, D. Zhao, Q. Wang, Aggregation of carboxyl-modified polystyrene nanoplastics in water with aluminum chloride: Structural characterization and theoretical calculation, *Water Res* 208 (2022) 117884, <https://doi.org/10.1016/j.watres.2021.117884>.
- [4] E. Tiwari, N. Singh, N. Khandelwal, F.A. Monikh, G.K. Darbha, Application of Zn/Al layered double hydroxides for the removal of nano-scale plastic debris from aqueous systems, *J. Hazard. Mater.* 397 (2020) 122769, <https://doi.org/10.1016/j.jhazmat.2020.122769>.
- [5] F. Xiao, L.-J. Feng, X.-D. Sun, Y. Wang, Z.-W. Wang, F.-P. Zhu, X.-Z. Yuan, Do polystyrene nanoplastics have similar effects on duckweed (*Lemna minor L.*) at environmentally relevant and observed-effect concentrations? *Environ. Sci. Technol.* 56 (2022) 4071–4079, <https://doi.org/10.1021/acs.est.1c06595>.
- [6] R. Zhou, D. Zhou, S. Yang, Z. Shi, H. Pan, Q. Jin, Z. Ding, Neurotoxicity of polystyrene nanoplastics with different particle sizes at environment-related concentrations on early zebrafish embryos, *Sci. Total Environ.* 872 (2023) 162096, <https://doi.org/10.1016/j.scitotenv.2023.162096>.
- [7] Z. Li, L. Yan, M. Junaid, X. Chen, H. Liao, D. Gao, Q. Wang, Y. Zhang, J. Wang, Impacts of polystyrene nanoplastics at the environmentally relevant and sub-lethal concentrations on the oxidative stress, immune responses, and gut microbiota to grass carp (*Ctenopharyngodon idella*), *J. Hazard. Mater.* 441 (2023) 129995, <https://doi.org/10.1016/j.jhazmat.2022.129995>.
- [8] M. Yao, L. Mu, Z. Gao, X. Hu, Persistence of algal toxicity induced by polystyrene nanoplastics at environmentally relevant concentrations, *Sci. Total Environ.* 876 (2023) 162853, <https://doi.org/10.1016/j.scitotenv.2023.162853>.
- [9] L. Liu, H. Zheng, L. Luan, X. Luo, X. Wang, H. Lu, Y. Li, L. Wen, F. Li, J. Zhao, Functionalized polystyrene nanoplastic-induced energy homeostasis imbalance and

the immunomodulation dysfunction of marine clams (*Meretrix meretrix*) at environmentally relevant concentrations, *Environ. Sci. Nano* 8 (2021) 2030–2048, <https://doi.org/10.1039/D1EN00212K>.

[10] Z.A. Ganie, N. Khandelwal, E. Tiwari, N. Singh, G.K. Darbha, Biochar-facilitated remediation of nanoplastic contaminated water: Effect of pyrolysis temperature induced surface modifications, *J. Hazard. Mater.* 417 (2021) 126096, <https://doi.org/10.1016/j.jhazmat.2021.126096>.

[11] X. Hua, D. Wang, Cellular Uptake, Transport, and Organelle Response After Exposure to Microplastics and Nanoplastics: Current Knowledge and Perspectives for Environmental and Health Risks, *Rev. Environ. Contam. Toxicol.* 260 (2022) 12, <https://doi.org/10.1007/s44169-022-00013-x>.

[12] V. Tolardo, A. Romaldini, F. Fumagalli, A. Armirotti, M. Veronesi, D. Magri, S. Sabella, A. Athanassiou, D. Fragouli, Polycarbonate nanoplastics and the in vitro assessment of their toxicological impact on liver functionality, *Environ. Sci. Nano* 10 (2023) 1413–1427, <https://doi.org/10.1039/D2EN00963C>.

[13] D. Magri, P. Sánchez-Moreno, G. Caputo, F. Gatto, M. Veronesi, G. Bardi, T. Catelan, D. Guarnieri, A. Athanassiou, P.P. Pompa, D. Fragouli, Laser ablation as a versatile tool to mimic polyethylene terephthalate nanoplastic pollutants: characterization and toxicology assessment, *ACS Nano* 12 (2018) 7690–7700, <https://doi.org/10.1021/acsnano.8b01331>.

[14] A. Katsumi, M.P. Losada-Carrillo, M. Barros, M.P. Cajaraville, Polystyrene nanoplastics and microplastics can act as Trojan horse carriers of benzo(a)pyrene to mussel hemocytes in vitro, *Sci. Rep.* 11 (2021) 22396, <https://doi.org/10.1038/s41598-021-01938-4>.

[15] D. Magri, M. Veronesi, P. Sánchez-Moreno, V. Tolardo, T. Bandiera, P.P. Pompa, A. Athanassiou, D. Fragouli, PET nanoplastics interactions with water contaminants and their impact on human cells, *Environ. Pollut.* 271 (2021) 116262, <https://doi.org/10.1016/j.envpol.2020.116262>.

[16] T.P. Wagner, Reducing single-use plastic shopping bags in the USA, *Waste Manag.* 70 (2017) 3–12, <https://doi.org/10.1016/j.wasman.2017.09.003>.

[17] D. Merino, A. Zych, A. Athanassiou, Biodegradable and Biobased Mulch Films: Highly Stretchable PLA Composites with Different Industrial Vegetable Waste, *ACS Appl. Mater. Interfaces* 14 (2022) 46920–46931, <https://doi.org/10.1021/acsami.2c10965>.

[18] N. Tiwari, D. Santhiya, J.G. Sharma, Microbial remediation of micro-nano plastics: Current knowledge and future trends, *Environ. Pollut.* 265 (2020) 115044, <https://doi.org/10.1016/j.envpol.2020.115044>.

[19] N. Zhu, Q. Yan, Y. He, X. Wang, Z. Wei, D. Liang, H. Yue, Y. Yun, G. Li, N. Sang, Insights into the removal of polystyrene nanoplastics using the contaminated corn cob-derived mesoporous biochar from mining area, *J. Hazard. Mater.* 433 (2022) 128756, <https://doi.org/10.1016/j.jhazmat.2022.128756>.

[20] Y. Xiong, J. Zhao, L. Li, Y. Wang, X. Dai, F. Yu, J. Ma, Interfacial interaction between micro/nanoplastics and typical PPCPs and nanoplastics removal via electro sorption from the aqueous solution, *Water Res.* 184 (2020) 116100, <https://doi.org/10.1016/j.watres.2020.116100>.

[21] Y. Zhang, A. Diehl, A. Lewandowski, K. Gopalakrishnan, T. Baker, Removal efficiency of micro- and nanoplastics (180 nm–125 µm) during drinking water treatment, *Sci. Total Environ.* 720 (2020) 137383, <https://doi.org/10.1016/j.scitotenv.2020.137383>.

[22] P.H. Allé, P. García-Muñoz, K. Adouby, N. Keller, D. Robert, Efficient photocatalytic mineralization of polymethylmethacrylate and polystyrene nanoplastics by TiO₂/β-SiC alveolar foams, *Environ. Chem. Lett.* 19 (2021) 1803–1808, <https://doi.org/10.1007/s10311-020-01099-2>.

[23] J.D. Acuña-Bedoya, E. Lluévano-Hipólito, E.I. Cedillo-González, L.P. Domínguez-Jaimes, A.M. Hurtado, J.M. Hernández-López, Boosting visible-light photocatalytic degradation of polystyrene nanoplastics with immobilized Cu_xO obtained by anodization, *J. Environ. Chem. Eng.* 9 (2021) 106208, <https://doi.org/10.1016/j.jece.2021.106208>.

[24] R.-C. Wang, Y.-C. Lin, H.-C. Chen, W.-Y. Lin, Energy harvesting from g-C₃N₄ piezoelectric nanogenerators, *Nano Energy* 83 (2021) 105743, <https://doi.org/10.1016/j.nanoen.2021.105743>.

[25] Y. He, L. Zhang, M. Fan, X. Wang, M.L. Walbridge, Q. Nong, Y. Wu, L. Zhao, Z-scheme SnO₂-g-C₃N₄ composite as an efficient photocatalyst for dye degradation and photocatalytic CO₂ reduction, *Sol. Energy Mater. Sol. Cells* 137 (2015) 175–184, <https://doi.org/10.1016/j.solmat.2015.01.037>.

[26] Y. Wang, Y. Xu, S. Dong, P. Wang, W. Chen, Z. Lu, D. Ye, B. Pan, D. Wu, C. D. Vecitis, G. Gao, Ultrasonic activation of inert poly(tetrafluoroethylene) enables piezocatalytic generation of reactive oxygen species, *Nat. Commun.* 12 (2021) 3508, <https://doi.org/10.1038/s41467-021-23921-3>.

[27] H. Lv, Y. Liu, P. Zhao, Y. Bai, W. Cui, S. Shen, Y. Liu, Z. Wang, D.-G. Yu, Insight into the superior piezophotocatalytic performance of BaTiO₃//ZnO Janus nanofibrous heterostructures in the treatment of multi-pollutants from water, *Appl. Catal. B Environ.* 330 (2023) 122623, <https://doi.org/10.1016/j.apcatb.2023.122623>.

[28] X. Zhou, Q. Sun, Z. Xiao, H. Luo, D. Zhang, Three-dimensional BNT/PVDF composite foam with a hierarchical pore structure for efficient piezo-photocatalysis, *J. Environ. Chem. Eng.* 10 (2022) 108399, <https://doi.org/10.1016/j.jece.2022.108399>.

[29] Y. Cui, Z. Wang, B. Li, Y. Yan, R. Xu, M. Meng, Y. Yan, Fluid-induced piezoelectric field enhancing photocatalytic hydrogen evolution reaction on g-C₃N₄/LiNbO₃/PVDF membrane, *Nano Energy* 99 (2022) 107429, <https://doi.org/10.1016/j.nanoen.2022.107429>.

[30] K. Manikandan, S. Dhanuskodi, A.Rose Thomas, N. Maheswari, G. Muralidharan, D. Sastikumar, Size-strain distribution analysis of SnO₂ nanoparticles and their multifunctional applications as fiber optic gas sensors, supercapacitors and optical limiters, *RSC Adv.* 6 (2016) 90559–90570, <https://doi.org/10.1039/C6RA20503H>.

[31] H. Lei, Q. He, M. Wu, Y. Xu, P. Sun, X. Dong, Piezoelectric polarization promoted spatial separation of photoexcited electrons and holes in two-dimensional g-C₃N₄ nanosheets for efficient elimination of chlorophenols, *J. Hazard. Mater.* 421 (2022) 126696, <https://doi.org/10.1016/j.jhazmat.2021.126696>.

[32] N. Pourshirband, A. Nezamzadeh-Ejhieh, An efficient Z-scheme CdS/g-C₃N₄ nano catalyst in methyl orange photodegradation: Focus on the scavenging agent and mechanism, *J. Mol. Liq.* 335 (2021) 116543, <https://doi.org/10.1016/j.molliq.2021.116543>.

[33] L. Haryński, A. Olejnik, K. Grochowska, K. Siuzdak, A facile method for Tauc exponent and corresponding electronic transitions determination in semiconductors directly from UV-Vis spectroscopy data, *Opt. Mater.* 127 (2022) 112205, <https://doi.org/10.1016/j.optmat.2022.112205>.

[34] J. Tauc, R. Grigorovici, A. Vancu, Optical properties and electronic structure of amorphous germanium, *Phys. Status Solidi B* 15 (1966) 627–637, <https://doi.org/10.1002/pssb.19660150224>.

[35] C. Zhou, Y. Yang, G. Wu, M. Mu, X. Yin, 2D Cu-FeTCPP MOF assembled on ZnTi-LDH to construct 2D/2D direct Z-scheme heterojunction for enhanced photocatalytic CO₂ reduction, *Sol. Energy* 253 (2023) 480–490, <https://doi.org/10.1016/j.solener.2023.02.058>.

[36] M.S. Athar, M. Danish, M. Muneeb, Fabrication of visible light-responsive dual Z-Scheme (α-Fe₂O₃/CdS/g-C₃N₄) ternary nanocomposites for enhanced photocatalytic performance and adsorption study in aqueous suspension, *J. Environ. Chem. Eng.* 9 (2021) 105754, <https://doi.org/10.1016/j.jece.2021.105754>.

[37] A. Khataee, A. Fazli, M. Fathinia, F. Vafaei, Removal of diatom *Nitzschia* sp. cells via ozonation process catalyzed by martite nanoparticles, *J. Clean. Prod.* 186 (2018) 475–489, <https://doi.org/10.1016/j.jclepro.2018.03.136>.

[38] A. Fazli, F. Zakeri, A. Khataee, Y. Orooji, A BaTiO₃/WS₂ composite for piezo-photocatalytic persulfate activation and ofloxacin degradation, *Commun. Chem.* 5 (1) (2022) 14, <https://doi.org/10.1038/s42004-022-00707-2>.

[39] F. Fina, S.K. Callear, G.M. Carins, J.T.S. Irvine, Structural investigation of graphitic carbon nitride via XRD and neutron diffraction, *Chem. Mater.* 27 (2015) 2612–2618, <https://doi.org/10.1021/acs.chemmater.5b00411>.

[40] H. Derikvandi, A. Nezamzadeh-Ejhieh, Synergistic effect of p-n heterojunction, supporting and zeolite nanoparticles in enhanced photocatalytic activity of NiO and SnO₂, *J. Colloid Interface Sci.* 490 (2017) 314–327, <https://doi.org/10.1016/j.jcis.2016.11.069>.

[41] M. Choi, W. Tong, Z. Wang, Z. Chen, Y. An, Y. Zhang, Piezoelectric-Fenton degradation and mechanism study of Fe₂O₃/PVDF-HFP porous film drove by flowing water, *J. Hazard. Mater.* 430 (2022) 128446, <https://doi.org/10.1016/j.jhazmat.2022.128446>.

[42] S. Tazikeh, A. Akbari, A. Talebi, E. Talebi, Synthesis and characterization of tin oxide nanoparticles via the Co-precipitation method, *Mater. Sci. -Pol.* 32 (2014) 98–101, <https://doi.org/10.2478/s13536-013-0164-y>.

[43] K. Nejati, Synthesis by precipitation method and investigation of SnO₂ nanoparticles, *Cryst. Res. Technol.* 47 (2012) 567–572, <https://doi.org/10.1002/crat.201100633>.

[44] Y. Zang, L. Li, X. Li, R. Lin, G. Li, Synergistic collaboration of g-C₃N₄/SnO₂ composites for enhanced visible-light photocatalytic activity, *Chem. Eng. J.* 246 (2014) 277–286, <https://doi.org/10.1016/j.cej.2014.02.068>.

[45] A. Mohammad, M.R. Karim, M.E. Khan, M.M. Khan, M.H. Cho, Biofilm-Assisted Fabrication of Ag@SnO₂-g-C₃N₄ Nanostructures for Visible Light-Induced Photocatalysis and Photoelectrochemical Performance, *J. Phys. Chem. C* 123 (2019) 20936–20948, <https://doi.org/10.1021/acs.jpcc.9b05105>.

[46] Z. Sha, C. Boyer, G. Li, Y. Yu, F.-M. Alliouxe, K. Kalantar-Zadeh, C.-H. Wang, J. Zhang, Electrospun liquid metal/PVDF-HFP nanofiber membranes with exceptional triboelectric performance, *Nano Energy* 92 (2022) 106713, <https://doi.org/10.1016/j.nanoen.2021.106713>.

[47] K.N. Van, H.T. Huu, V.N. Nguyen Thi, T.L. Le Thi, D.H. Truong, T.T. Truong, N. N. Dao, V. Vo, D.L. Tran, Y. Vasseghian, Facile construction of S-scheme SnO₂/g-C₃N₄ photocatalyst for improved photoactivity, *Chemosphere* 289 (2022) 133120, <https://doi.org/10.1016/j.chemosphere.2021.133120>.

[48] Y.-L. Wang, Y. Tian, Z.-L. Lang, W. Guan, L.-K. Yan, A highly efficient Z-scheme B-doped g-C₃N₄/Sn₂ photocatalyst for CO₂ reduction reaction: a computational study, *J. Mater. Chem. A* 6 (2018) 21056–21063, <https://doi.org/10.1039/C8TA07352J>.

[49] X. Wang, Y. Li, J. Zhao, X. Xia, X. Shi, J. Duan, W. Zhang, UV-induced aggregation of polystyrene nanoplastics: effects of radicals, surface functional groups and electrolyte, *Environ. Sci. Nano* 7 (2020) 3914–3926, <https://doi.org/10.1039/DOEN00518E>.

[50] S. Jiang, M. Yin, H. Ren, Y. Qin, W. Wang, Q. Wang, X. Li, Novel CuMgAl₂-LDH Photocatalyst for Efficient Degradation of Microplastics under Visible Light Irradiation, *Polymers* 15 (2023) 2347, <https://doi.org/10.3390/polym15102347>.

[51] K. Bhagat, A.C. Barrios, K. Rajwade, A. Kumar, J. Oswald, O. Apul, F. Perreault, Aging of microplastics increases their adsorption affinity towards organic contaminants, *Chemosphere* 298 (2022) 134238, <https://doi.org/10.1016/j.chemosphere.2022.134238>.

[52] P. García-Muñoz, P.H. Allé, C. Bertoloni, A. Torres, M.U. de la Orden, J.M. Urreaga, M.-A. Dziurla, F. Fresno, D. Robert, N. Keller, Photocatalytic degradation of polystyrene nanoplastics in water. A methodological study, *J. Environ. Chem. Eng.* 10 (2022) 108195, <https://doi.org/10.1016/j.jece.2022.108195>.

[53] S. Dong, X. Yan, Y. Yue, W. Li, W. Luo, Y. Wang, J. Sun, Y. Li, M. Liu, M. Fan, H₂O₂ concentration influenced the photoaging mechanism and kinetics of polystyrene microplastic under UV irradiation: Direct and indirect photolysis, *J. Clean. Prod.* 380 (2022) 135046, <https://doi.org/10.1016/j.jclepro.2022.135046>.

[54] R.M. France, R.D. Short, Plasma treatment of polymers: the effects of energy transfer from an argon plasma on the surface chemistry of polystyrene, and polypropylene. a high-energy resolution x-ray photoelectron spectroscopy study, *Langmuir* 14 (1998) 4827–4835, <https://doi.org/10.1021/la9713053>.

[55] O.M. Ba, P. Marmey, K. Anselme, A.C. Duncan, A. Ponche, Surface composition XPS analysis of a plasma treated polystyrene: evolution over long storage periods, *Colloids Surf. B Biointerfaces* 145 (2016) 1–7, <https://doi.org/10.1016/j.colsurfb.2016.04.026>.

[56] Y. Li, J. Li, J. Ding, Z. Song, B. Yang, C. Zhang, B. Guan, Degradation of nano-sized polystyrene plastics by ozonation or chlorination in drinking water disinfection processes, *Chem. Eng. J.* 427 (2022) 131690, <https://doi.org/10.1016/j.cej.2021.131690>.

[57] C. Zhang, W. Fei, H. Wang, N. Li, D. Chen, Q. Xu, H. Li, J. He, J. Lu, p-n Heterojunction of BiOI/ZnO nanorod arrays for piezo-photocatalytic degradation of bisphenol A in water, *J. Hazard. Mater.* 399 (2020) 123109, <https://doi.org/10.1016/j.jhazmat.2020.123109>.

[58] W. Wu, X. Yin, B. Dai, J. Kou, Y. Ni, C. Lu, Water flow driven piezo-photocatalytic flexible films: Bi-piezoelectric integration of ZnO nanorods and PVDF, *Appl. Surf. Sci.* 517 (2020) 146119, <https://doi.org/10.1016/j.apsusc.2020.146119>.

[59] X. Liu, S. Xu, X. Kuang, D. Tan, X. Wang, Nanoscale investigations on β -phase orientation, piezoelectric response, and polarization direction of electrospun PVDF nanofibers, *RSC Adv.* 6 (2016) 109061–109066, <https://doi.org/10.1039/C6RA24473D>.

[60] X. Liu, J. Ma, X. Wu, L. Lin, X. Wang, Polymeric nanofibers with ultrahigh piezoelectricity via self-orientation of nanocrystals, *ACS Nano* 11 (2017) 1901–1910, <https://doi.org/10.1021/acsnano.6b07961>.

[61] L. Song, S. Sun, S. Zhang, J. Wei, Hydrogen production and mechanism from water splitting by metal-free organic polymers PVDF/PVDF-HFP under drive by vibrational energy, *Fuel* 324 (2022) 124572, <https://doi.org/10.1016/j.fuel.2022.124572>.

[62] X. Zhao, Z. Li, J. Yu, C. Li, S. Xu, F. Li, C. Zhang, B. Man, C. Zhang, Plasmonic and bi-piezoelectric enhanced photocatalysis using PVDF/ZnO/Au nanobrush, *Nanophotonics* 11 (2022) 3339–3349, <https://doi.org/10.1515/nanoph-2022-0194>.

[63] X. Liao, X. Chen, Y. Tang, M. Zhu, H. Xie, Y. Xin, Y. Lin, X. Fan, Enhanced piezocatalytic reactive oxygen species production activity and recyclability of the dual piezoelectric Cu3B2O6/PVDF composite membrane, *ACS Appl. Mater. Interfaces* 15 (2023) 1286–1295, <https://doi.org/10.1021/acsami.2c19083>.

[64] M. Li, J. Sun, G. Chen, S. Yao, B. Cong, Construction double electric field of sulphur vacancies as medium ZnS/Bi₂S₃-PVDF self-supported recoverable piezoelectric film photocatalyst for enhanced photocatalytic performance, *Appl. Catal. B Environ.* 301 (2022) 120792, <https://doi.org/10.1016/j.apcatb.2021.120792>.

[65] A. Khataee, A. Fazli, M. Fathinia, F. Vafaei, Simultaneous elimination of two species of algae from a contaminated water through ozonation process: mechanism and destruction intermediates, *Ozone Sci. Eng.* 41 (2019) 35–45, <https://doi.org/10.1080/01919512.2018.1480931>.

[66] A.D. Vital-Grappin, M.C. Ariza-Tarazona, V.M. Luna-Hernández, J.F. Villarreal-Chiu, J.M. Hernández-López, C. Siligardi, E.I. Cedillo-González, The role of the reactive species involved in the photocatalytic degradation of HDPE microplastics using C,N-TiO₂ powders, *Polymers* 13 (2021) 999, <https://doi.org/10.3390/polym13070999>.